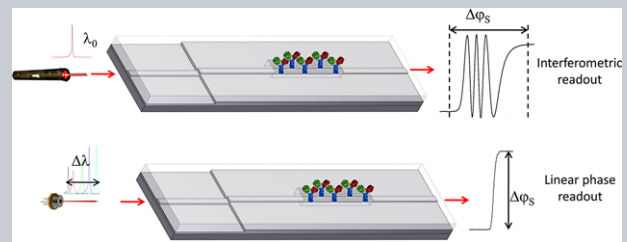


This is the peer reviewed version of the following article:

Dante S., Duval D., Fariña D., González-Guerrero A.B.,
Lechuga L.M.. Linear readout of integrated interferometric
biosensors using a periodic wavelength modulation. *Laser and
Photonics Reviews*, (2015). 9. : 248 - .
10.1002/lpor.201400216,

which has been published in final form at
<https://dx.doi.org/10.1002/lpor.201400216>. This article may
be used for non-commercial purposes in accordance with
Wiley Terms and Conditions for Use of Self-Archived Versions.

Abstract An all-optical phase modulation method for the linear readout of integrated interferometric biosensors is demonstrated, merging simple intensity detection with the advantages offered by spectral interrogation. The phase modulation is introduced in a simple and cost-effective way by tuning a few nanometers the emission wavelength of commercial laser diodes, taking advantage of their well-known drawback of power–wavelength dependence. The method is applied to the case of a bimodal waveguide (BiMW) interferometric biosensor, fabricated with standard silicon technology and operated at visible wavelengths, rendering a detection limit of 4×10^{-7} refractive index units for bulk sensing. The biosensing capabilities of the phase-linearized BiMW



device are assessed through the quantitative immunoassay of C-reactive protein, a key protein in inflammatory processes. This method can be applied to any modal interferometer.

Linear readout of integrated interferometric biosensors using a periodic wavelength modulation

Stefania Dante, Daphné Duval, David Fariña, Ana Belén González-Guerrero, and Laura M. Lechuga*

1. Introduction

Integrated optics-based biosensors are highly sensitive analytical platforms as required in clinical, pharmaceutical, or industrial fields. They offer compelling advantages such as label-free detections, reduction of sample and reagent volume, and very small dimensions which allow easy multiplexing and large-scale production, resulting in a reduced cost of the final product. Among them, interferometric arrangements have demonstrated the highest sensitivity, with detection limits in the range 10^{-8} – 10^{-7} refractive index units (RIU) for bulk detection and 10^{-9} – 10^{-8} RIU for surface sensing [1, 2].

The most commonly employed configurations are based on two-path arrangements such as Mach–Zehnder [3, 4], Young [5–7], or Hartman interferometers [8, 9], where the interference between the two propagating beams is recorded either as an intensity variation or as a displacement of the interference pattern.

As an alternative to double-path interferometers, single-path configurations offer simplified fabrication and compact footprint, since the necessity of lateral beam splitting and recombination is suppressed. In the general scheme, two modes of different order or polarization propagate in the same channel. They both probe the sample solution but with different sensitivities, a consequence of their distinct confinement factors. The resulting relative phase difference can be evaluated as a variation of the far-field pattern created at the device output or as an intensity variation by

introducing a single-mode recombination section [10]. The first devices were implemented with optical fibers [11–15] and the principle was later transferred to photonic crystal fibers [16, 17] and integrated optics, as in the case of the bimodal waveguide (BiMW) device [18] developed by our group, where two transverse modes of different orders propagate in the same straight waveguide.

However, despite the wide range of geometries and configurations that have been presented, a full applicability of interferometric biosensors is still missing, mainly due to the complex readout of the interferometric response. The periodic dependence of the output intensity introduces ambiguities in the evaluation of the sensor response, such as direction ambiguities, direction ambiguity, and sensitivity fading.

In order to overcome the drawbacks of the periodic readout, several approaches have been suggested to translate the standard interferometric detection scheme into an unambiguous linear phase evaluation. These approaches are mainly based on phase compensation or modulation techniques, introduced through different principles such as electro-optic [19–21], thermo-optic [22], magneto-optic [23], liquid crystals [24], or photosensitive layers [25]. More recently a coherent detection scheme was proposed by Halir *et al.* [26] to unambiguously extract the phase signal from an integrated Mach–Zehnder interferometer (MZI) modified with a three-waveguide output coupler. Other strategies to overcome these limitations rely on spectral interrogation [17, 27–30], where a shift of the interference

pattern occurs in response to a refractive index variation, similarly to the working principle of optical resonators [31]. But for any of these approaches to be implemented, additional fabrication processes or bulky equipment, such as tunable lasers or spectrometers, are required to achieve a linear phase readout.

We recently introduced a simple and cost-effective phase modulation technique which does not require any additional fabrication processes or external equipment. This technique, previously applied to MZI geometry [32], employs a periodic modulation of the incident wavelength, achieved with common laser diodes, and Fourier deconvolution of the modulated signal to retrieve the phase information.

In this work our main goal is to demonstrate the validity of the method for all modal interferometers by considering two generic modes in a mathematical model. The method can then be directly applied to a specific device by assessing the dispersion relations of the modes of interest, which are determined by the configuration, materials, wavelength, and polarization. Here we chose a silicon-based single-path interferometer, the BiMW device, as a model case where two transverse modes of different orders are involved. In Section 2, the working principle of modal interferometers is presented, including the limitations of traditional monochromatic interrogation and the critical effects arising from spectral interrogation. Then, in Section 3, the mathematical modeling of the wavelength modulation approach is described for a generic interferometric output. Section 4 details the experimental implementation and the bulk calibration of the wavelength-modulated BiMW, along with a biosensing proof-of-concept through the detection of the C-reactive protein using a direct immunoassay.

2. Sensor working principle

The BiMW interferometer is constituted of a single-mode input waveguide followed by a thicker waveguide where two modes of different orders (fundamental and first order) propagate to the end of the device [18]. Due to their different confinement factors, the first-order mode is mainly responsible for the sensing of changes occurring on the device surface while the fundamental mode can be considered as a virtual reference.

A schematic view of the device is shown in Fig. 1. To ensure single-mode behavior in the longitudinal direction in the visible, a nanometric height rib waveguide ($4 \mu\text{m}$ width \times 1.5 nm height) is defined over a Si_3N_4 core layer (150 nm for the single-mode section and $300\text{--}350 \text{ nm}$ for the bimodal part) embedded between two SiO_2 cladding layers ($1.5 \mu\text{m}$ thickness). In the bimodal section, a portion of the cladding is removed, defining a sensing area where the evanescent field of the guided light can probe the environment. Considering the propagation over a length L , the

phase difference between the two modes is given by

$$\Delta\varphi(\lambda, n) = 2\pi \frac{L}{\lambda} (N_1(\lambda, n) - N_0(\lambda, n)) \quad (1)$$

$$= 2\pi \frac{L}{\lambda} \Delta N_{\text{eff}}(\lambda, n), \quad (2)$$

where N_0 and N_1 are the effective refractive indices of the two propagating modes, respectively, ΔN_{eff} their difference, and λ the working wavelength. Equation (2) is the general expression of the phase difference between the two propagating modes in any interferometer (double- and single-path), independently of the readout scheme (intensity or far-field distribution detection).

In the case of BiMW, the superposition of the two modes at the device output results in a two-lobe intensity distribution that depends on the phase difference accumulated across the whole bimodal length. The temporal evolution of this phase difference is quantified by the monitoring of the signal S_R , given by

$$S_R = \frac{I_{\text{up}} - I_{\text{down}}}{I_{\text{up}} + I_{\text{down}}} \propto V \cos(\Delta\varphi), \quad (3)$$

where I_{up} and I_{down} are the currents measured by the upper and lower sections respectively of a two-section photodiode and V is the visibility factor. V represents the amplitude of the output variations (fringe amplitude) and it is determined by the coupling coefficients which govern the mode power splitting taking place at the step junction. In the monochromatic approach, we experimentally obtain visibility factors in the range $50\text{--}70\%$ depending on the bimodal core thicknesses ($300\text{--}350 \text{ nm}$) and on the working wavelength ($600\text{--}700 \text{ nm}$). As S_R is normalized to the total power propagating in the structure, it is immune to input fluctuations due to laser or mechanical instabilities, preventing false-positive responses.

As the phase variation is deduced from the variations of S_R , the device sensitivity to refractive index changes is given by

$$\frac{\partial S_R}{\partial n} = \frac{\partial S_R}{\partial \Delta\varphi} \frac{\partial \Delta\varphi}{\partial n}. \quad (4)$$

As shown in Fig. 2, the curves of the phase sensitivity $\partial \Delta\varphi / \partial n$ computed from Eq. (2) as a function of the bimodal core thickness for a sensing area length $L_{\text{SA}} = 15 \text{ nm}$ and a working wavelength $\lambda_0 = 660 \text{ nm}$ show maximum values for core thicknesses of 310 nm for TE polarization and 375 nm for TM polarization, corresponding respectively to $2510 \times 2\pi$ and $3270 \times 2\pi \text{ rad/RIU}$.

It should be noted that the device sensitivity expressed by Eq. (4) is slightly lower than the calculated phase sensitivity due to the presence of the term $\partial S_R / \partial \Delta\varphi \propto V \sin(\Delta\varphi)$ which depends on the visibility V of the fringe pattern and on the initial value of the phase difference between the two propagating modes. This dependence of the sensitivity on the phase difference value, referred to as sensitivity fading, constitutes one of the main limitations of

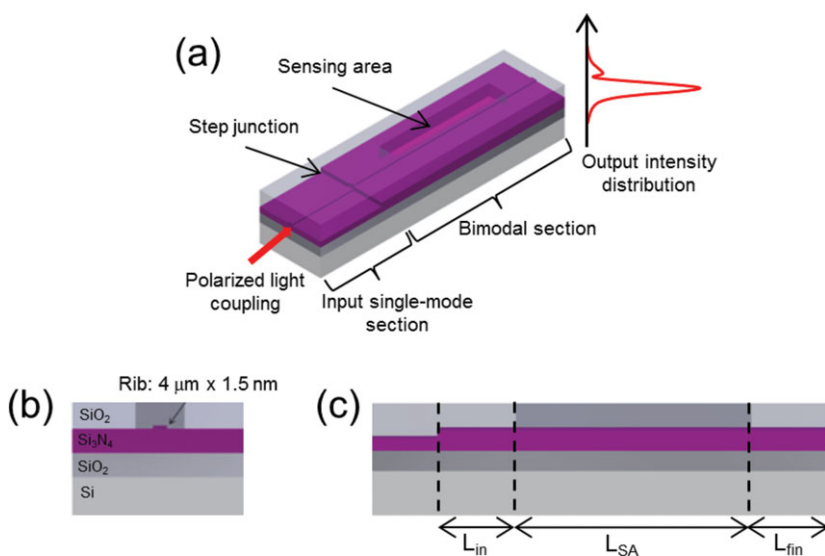


Figure 1 Device scheme: (a) general sensor view with main components, (b) waveguide cross-section, and (c) longitudinal view.

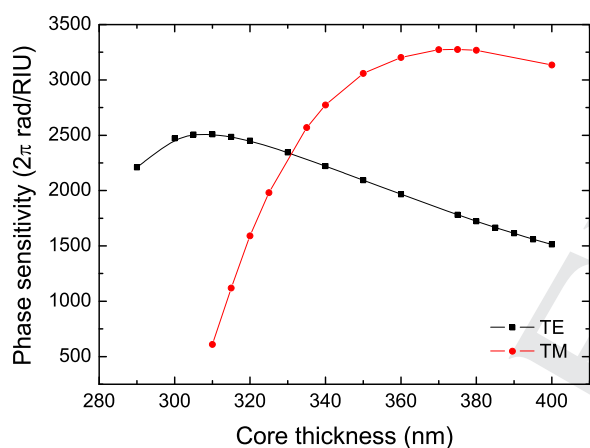


Figure 2 Bulk sensitivity as a function of core thickness, for TE and TM polarizations, for a central wavelength $\lambda_0 = 660$ nm.

the traditional intensity interrogation scheme. This drawback can be overcome by introducing alternative readout schemes, as demonstrated in this work.

A sinusoidal dependence is generally assumed between the phase variation and the wavelength; however, due to the different relations of dispersion of the involved modes, a critical point can arise when the function $\Delta N_{\text{eff}}(\lambda)/\lambda$ shows an extremum [33]. As a consequence, the sensitivity of spectrally interrogated interferometric sensors diverges in proximity of the critical point rendering potentially ultrahigh-sensitivity detections, limited only by the system noise [17, 33].

Figure 3 a shows the behavior of the function $\Delta N_{\text{eff}}(\lambda)/\lambda$ in the case of the BiMW device, with a bimodal core thickness of 340 nm and TE polarization. The curves are computed through two-dimensional simulations of the device cross-section, considering two different cases for the medium in contact with the sensing area. In the first case the medium is a silicon dioxide cladding ($n = 1.46$), resulting in a critical wavelength of around 665 nm (black curve), while in the case of water medium ($n = 1.33$) the

critical wavelength is shifted to 685 nm (red curve). To assess the effective critical wavelength of the device, the propagation along the complete structure is computed and the resulting transmission curve S_R is shown in Fig. 3 b: the critical point occurs for an effective critical wavelength of 676 nm, intermediate between the previous values of 665 and 685 nm. In Fig. 3 b we can notice how the periodic oscillations of $S_R(\lambda)$ are interrupted around the critical point and a smoother transition takes place.

It should be mentioned that during our studies we found that the rib dimensions, crucial for single-mode lateral behavior, do not lead to substantial variations for the critical effects, the core thickness being the dominant parameter.

Because they are a consequence of modal dispersion, critical effects are more evident for single-path interferometers than for standard two-path configurations where the same order dispersion relation governs both sensing and reference modes and the phase accumulation only takes place in the sensing area.

In the frame of intensity interrogation, i.e. constant wavelength, it is more convenient to study the critical behavior in terms of critical thickness for a given working wavelength. In the case of the BiMW sensor operated at 660 nm, the critical thickness is found to be around 330 nm. Out of the critical range, a sinusoidal dependence can be assumed for small wavelength variations.

3. All-optical phase modulation method

In order to solve the problems of the periodic sensor response and the resulting phase ambiguities, a modification of the phase difference between the two propagating modes can be introduced by altering their effective indices through small variations of the propagating wavelength. If this variation is introduced in a periodic manner, Fourier transform deconvolution can be applied, allowing one to directly access the phase information and furthermore to filter out noise contributions at a frequency different from the modulation frequency and its harmonics.

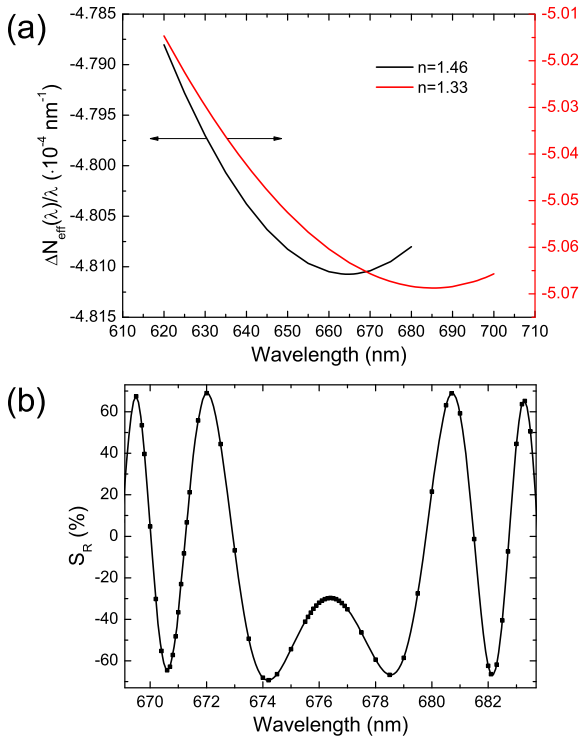


Figure 3 Critical effects for 340 nm core thickness and TE polarization. (a) Plots of $\Delta N_{\text{eff}}(\lambda)/\lambda$ for $n = 1.33$ and $n = 1.46$ obtained with modal analysis. (b) BiMW transfer function for $n = 1.33$ in the sensing area obtained with far-field analysis. Single-mode core thickness is 150 nm.

Under the hypothesis of sinusoidal phase modulation $f(\omega) = \mu \sin(\omega t)$ applied to a sinusoidal transfer function $S(\Delta\varphi)$, we obtain a modulated output signal of the type

$$S(\Delta\varphi) = V \cdot \cos[\Delta\varphi + \mu \sin(\omega t)], \quad (5)$$

where ω is the modulation frequency and μ the modulation depth. In the Fourier domain, the signal harmonics are given by

$$I_{2n} = 2V \cdot \cos(\Delta\varphi(t)) \cdot J_{2n}(\mu) \quad (6)$$

$$I_{2n+1} = 2V \cdot \sin(\Delta\varphi(t)) \cdot J_{2n+1}(\mu), \quad (7)$$

where $J_n(\mu)$ is a Bessel function of the first kind of order n , the amplitude of which depends on the modulation depth.

The phase shift information can therefore be directly and unambiguously retrieved from the expression

$$\Delta\varphi(t) = \arctan \frac{I_{2n+1}(\mu, \Delta\varphi(t))}{I_{2n}(\mu, \Delta\varphi(t))} \quad (8)$$

$$\text{if } J_{2n+1}(\mu) = J_{2n}(\mu). \quad (9)$$

With our approach, the sensitivity fading is solved since the phase information is retrieved from two signal

harmonics of different order, I_{2n} and I_{2n+1} , which show dependence on the phase difference, $\Delta\varphi$, of the type $\cos(\Delta\varphi)$ and $\sin(\Delta\varphi)$, respectively. Their sensitivities will therefore show alternated maxima and minima, which compensate each other along the phase variation.

For our application we chose the harmonics pair I_2 and I_3 since the low modulation depth required to satisfy Eq. (9), verified for $\mu = 1.2\pi$, can be easily introduced experimentally.

In the context of the proposed all-optical modulation scheme, the theoretical phase modulation depth μ must be related to a particular wavelength shift $\Delta\lambda_M$ of the laser diode, which depends on the specific interferometer geometry, the constituent materials, and the working wavelength through the mode dispersion relations. For any device section of arbitrary length L , the variation of the phase difference between the propagating modes $\delta(\Delta\varphi)$ induced by a small change $\delta\lambda$ of the propagating wavelength can be obtained by differentiating the general phase expression (2).

By making explicit the required wavelength change as a function of the induced phase shift we obtain

$$\delta\lambda = \frac{\delta(\Delta\varphi)}{2\pi L \left[-\frac{1}{\lambda^2} \Delta N_{\text{eff}} + \frac{1}{\lambda} \frac{\partial \Delta N_{\text{eff}}}{\partial \lambda} \right]}, \quad (10)$$

which is the general equation valid for any modal interferometer once the mode nature is specified through ΔN_{eff} and the geometry by L . In the case of dual-path interferometers operating far from the critical point, as in our previous study [32], as the two modes of interest have the same order dispersion relation, the term $\partial \Delta N_{\text{eff}} / \partial \lambda$ can be neglected, resulting in simplified expressions of Eq. (10).

However, considering the complete expression of Eq. (10), critical effects can appear as a consequence of the spectral interrogation when the denominator equals zero. For the BiMW geometry, the contributions of Eq. (10) from the three sections L_{in} , L_{SA} , and L_{fin} (see Fig. 1) must be taken into account. The resulting modulation depth $\Delta\lambda_M$ required to satisfy Eq. (9) and to achieve phase linearization when a water medium is present in the sensing area is shown in Fig. 4 for the case of TE polarization and a central wavelength $\lambda_0 = 660$ nm.

As we can observe, the required modulation amplitude diverges in correspondence of the critical thickness ($t \approx 330$ nm for $\lambda_0 = 660$ nm). Similar behavior is observed for TM polarization. In this case the divergence of the required modulation depth is observed for a thickness $t \approx 410$ nm (data not shown). Taking into account the limited operation range of the laser diode (approximately ± 0.5 nm), we can set boundaries which determine three regions: (i) sensor chips with bimodal part thickness lower than the critical value, (ii) sensor chips with waveguide thickness around the critical point, and (iii) sensor chips with waveguide thickness above the critical point. Sensor chips from family (ii) cannot be modulated with the proposed method: the required modulation depth diverges and cannot be introduced with our experimental approach. Sensor chips from families (i) and (iii) can be modulated

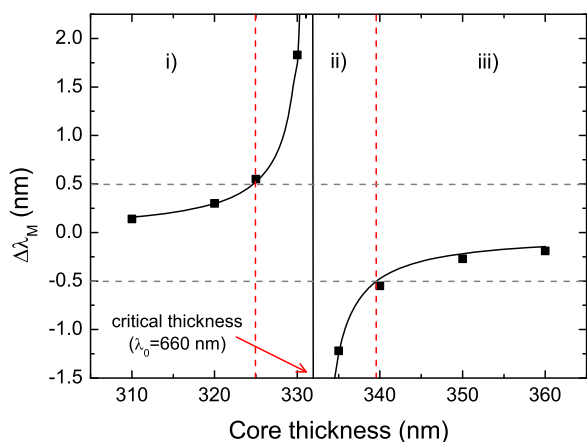


Figure 4 Required modulation depth as a function of bimodal core thickness. $\lambda_0 = 660$ nm, TE polarization.

and will show opposite directions for the phase variation in response to the same index change, due to the different signs of the required modulation depth. This change in the sensor response direction is in agreement with previous studies with hetero-modal fiber sensors [34, 35] which showed a similar critical behavior for a given wavelength.

For an optimized sensor design, the bimodal core thickness is chosen by considering sensitivity maximization and the applicability of the wavelength modulation approach. In the following we experimentally study the behavior of sensor chips belonging to the three different regions of Fig. 4.

4. Results and discussion

4.1. Experimental implementation

The sensor chip is placed over a custom-made, temperature-controlled chuck (T-resolution = 0.01°C). End-fire coupling of polarized light from a fiber pigtailed laser diode (LP660SF60, $\lambda_0 = 660$ nm, Thorlabs) with controlled temperature and current is achieved by employing a three-axis stage platform. An optical isolator is used to protect the laser cavity from unwanted reflections and to select the polarization. For this experiment, TE polarization is considered. A two-section detector is directly anchored in proximity of the waveguide output through a customized holder. Its vertical position is adjusted to ensure a symmetric S_R pattern (i.e. centered around zero) and maximum visibility. The intensity signals are amplified by commercial photodiode amplifiers, recorded with an acquisition card, and processed in real time.

For optical characterization a modulation frequency of 214 Hz is adopted since it allows one to resolve the changes of interest (time scale of minutes) and it is not affected by hardware limitations.

The theoretical requirements of the wavelength modulation depth are experimentally transferred to a condition on the amplitude of the laser driving current oscillations. A wavelength shift of 0.5 nm can be introduced with current

variations around ± 50 mA, which can usually be achieved by commercial laser diodes.

A custom-made Labview application is used for the generation of the input modulation signal and for the data acquisition process, synchronous with the input. A fast Fourier transform of the modulated output is computed in real time and the phase signal is evaluated from Eq. (8): the second and third harmonics are extracted from the real and imaginary portions of the Fourier spectrum respectively. After an unwrapping step to remove the 2π discontinuities, a continuous and monotonic signal is obtained in real time. As the BiMW output is normalized to the total power, there is no need for a reference signal to compensate for the amplitude modulation effects introduced by varying the laser driving current.

The deviations of the laser emission from an ideal case of perfect linear dependence on driving current and slight fabrication variations are overcome with a pre-set of the working point: the amplitude of the laser current oscillations is varied until the acquired harmonics oscillate in the same range, satisfying Eq. (9).

Figure 5 shows a comparison of the harmonic behavior during a variation of the refractive index in the sensing area for a sensor chip of family (i) modulated with a laser current amplitude $I_{LD} = \pm 28$ mA and a sensor chip of family

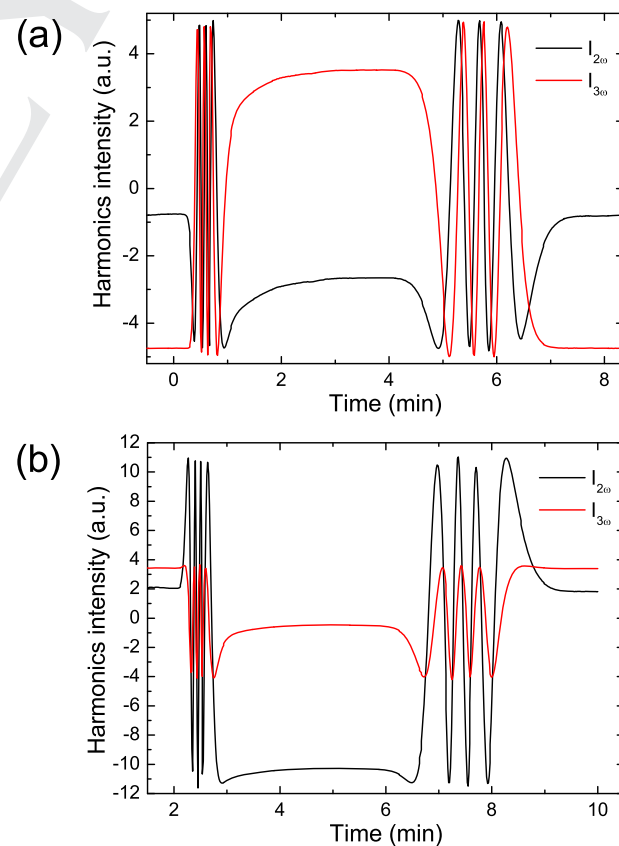


Figure 5 Comparison of the harmonic behavior in the case of (a) correct modulation set-point, achieved for a chip of family (i) and (b) insufficient modulation depth, observed for a chip of family (ii).

(ii) modulated with a current variation $I_{LD} = \pm 67$ mA. It can be noted how in the case of chip (i), operated at the correct working point, the second and third harmonics oscillate in the same range, while for chip (ii), despite the use of the maximum current excursion allowed, the amplitude of the oscillations of the second harmonic is larger than that of the third one. For this last chip the working point cannot be experimentally reached due to the divergence of the required modulation depth (compare Fig. 4).

For a given configuration, the critical region can be circumvented by modifying the central wavelength or the polarization of the incident beam. For instance, the chip of family (ii) could be modulated in TM polarization as in this case the critical region would be shifted to longer wavelengths.

4.2. Bulk sensing evaluation

For the demonstration of the phase modulation technique we chose two sensor chips with different core thicknesses: one belonging to group (i), with core thickness lower than the critical value; one belonging to group (iii), with core thickness higher than the critical value.

For the evaluation of the bulk refractive index sensitivity, different solutions of hydrochloric acid are sequentially supplied to the sensors through a fluidic system, while Milli-Q water is used as running buffer. A custom-made methacrylate cell with embedded polydimethylsiloxane channels allows access to a specific sensor in the chip, while a syringe pump maintains a constant flow regime. The refractive indices of the solutions are determined previously with an Abbe refractometer.

The insets in Fig. 6 show the temporal evolution of the sensor response when supplying different HCl solutions for

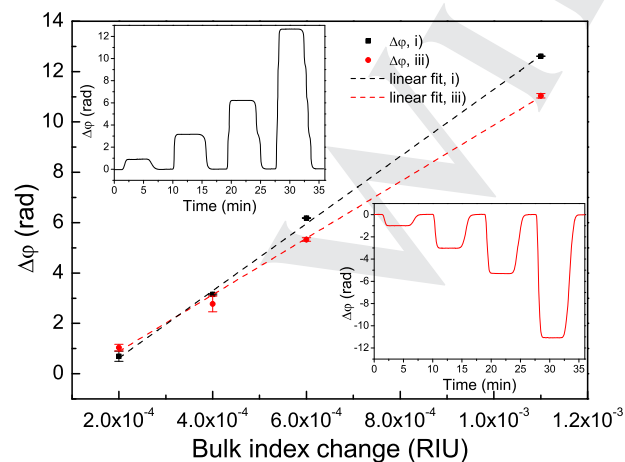


Figure 6 Calibration curves for the two sensor chips from families (i) and (iii), $\lambda_0 = 660$ nm, TE polarization. Insets show the temporal evolution of phase changes induced by different HCl concentrations. The opposite directions of the phase shifts are due to the sensor chip thicknesses and their relative position with respect to the critical point.

both sensor chips. The different signs for the modulation amplitude required according to Fig. 4 determine an upwards or downwards phase change for the same positive index variation, confirming theoretical expectations. The calibration curves, showing the phase change as a function of the index change are displayed in the main plot of Fig. 6. Experimental sensitivities are evaluated from the linear fit shown in Fig. 6, resulting in values of $2120 \times 2\pi$ rad/RIU for sensor chip (i) and $1790 \times 2\pi$ rad/RIU for sensor chip (iii), in agreement with the theoretical modeling. The experimentally measured sensitivities correspond to the device sensitivity expressed by Eq. (4) and are therefore slightly lower than the phase sensitivities presented in Fig. 2.

The limits of detection are evaluated assuming that the smallest detectable signal corresponds to three times the standard deviation on the baseline signal. Having standard deviations of 1.42 mrad for chip (i) and 2.45 mrad for chip (iii), we obtained limits of detection of 4×10^{-7} and 5.7×10^{-7} RIU for chips (i) and (iii) respectively. These values are comparable with the results achieved in the standard monochromatic approach employing a He-Ne laser [18], demonstrating the validity of the all-optical modulation method implemented with a standard laser diode.

4.3. Biosensing evaluation

For the validation of the wavelength-modulated BiMW as a biosensor we quantified the immunoreaction between the C-reactive protein (CRP) and its monoclonal antibody (C7 antibody), previously immobilized on the sensor chip surface. CRP is a cyclic pentameric protein produced by the liver, the concentration of which dramatically increases in the presence of inflammation or infections. It has been related to hypertension and cardiovascular diseases [36, 37], and is one of the biomarkers rapidly evaluated in health-care emergency units for any new incomer. The assay is implemented on the sensor chip from family (i), the most sensitive of the two sensor chips previously characterized in bulk.

Prior to antibody immobilization, the silicon nitride surface of the sensor is hydroxylated to expose -OH groups on the surface and silanized with a water-soluble silane, carboxyethylsilanetriol sodium salt, following the protocol detailed by González-Guerrero *et al.* [38]. The use of silanes as bridge elements between silicon-based transducers and biological molecules is well established since a stable covalent immobilization of specific bioreceptors occurs [1, 39]. The carboxylate groups are activated by 1-ethyl-3-(3-dimethylaminopropyl)carbodiimide hydrochloride/*N*-hydroxysuccinimide agents, allowing the covalent anchoring of the antibody, which is done *in situ* and monitored in real time. The specific antibody is supplied to the sensor surface, at a concentration of 20 $\mu\text{g/ml}$. A 1 M solution of ethanolamine (pH = 8.5) is used as blocking agent to deactivate unreacted carboxylic groups and prevent non-specific absorptions.

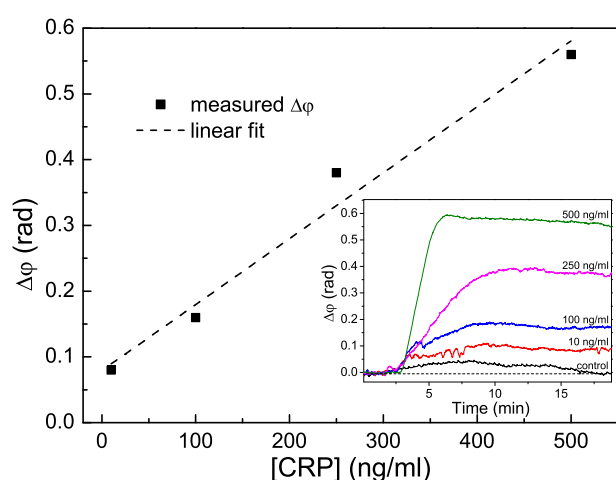


Figure 7 Dose–response curve for the direct assay detection of CRP. Inset shows the sensorgrams for the detection of various concentrations.

After stabilization of the bio-layer in phosphate-buffered saline (PBS) buffer, known concentrations of CRP diluted in PBS buffer in the range 10–500 ng/ml are supplied to the sensor, in a volume of 250 μ l. The corresponding sensorgrams are shown in the inset of Fig. 7. Regeneration of the bioreceptor layer after CRP immunodetection is done with 10 mM hydrochloric acid.

A control experiment is done by injecting a non-specific protein sample containing human chorionic gonadotropin hormone at a concentration of 1 μ g/ml, giving no appreciable signal, as demonstrated in the inset of Fig. 7.

From the data of the dose–response curve of Fig. 7 the detection limit is estimated as 7 ng/ml considering this value as the concentration inducing a signal equal to three times the baseline noise. This value, obtained with a direct and label-free immunoassay, is comparable to that of more complicated assay formats implemented for the same CRP/anti-CRP pair in other biosensor devices such as a surface plasmon resonance sensor [40] or electrochemical sensor [41] and satisfies the requirements of clinical application.

5. Conclusion and outlook

We demonstrated theoretically and experimentally a simple and cost-effective method to obtain a real-time linear signal as output, valid for any modal interferometer. The method is developed for a generic interferometric output, independent of the interferometric arrangement (single or double path) and of the readout approach (intensity or far-field pattern detection), resulting in a general approach which is later applied to the case of a BiMW sensor, where two transverse modes of different order propagate along the structure.

Careful design of the sensor chips is mandatory in order to overcome the critical effects arising from the difference between the dispersion relations of the involved modes. In proximity of the critical point a trade-off between

sensitivity maximization and feasibility of phase modulation is necessary. We demonstrated bulk detection limits of the order of 4×10^{-7} RIU and we presented a biosensing proof-of-concept for the immunoassay of the inflammatory biomarker C-reactive protein.

For future designs of interferometric biosensors, we believe that this wavelength-based modulation approach can offer a valid solution for bypassing interferometric limitations without increasing the complexity of design, fabrication, and measuring procedures. This offers a competitive solution for the implementation of lab-on-a-chip platforms employing interferometric biosensors, which can be commercialized in the near future.

Acknowledgements. This research was carried out with the financial support of EPISENS of the Spanish Ministry of Science and Innovation (TEC2012-34280). S. Dante acknowledges the Programa de Formación de Profesorado Universitario (FPU) of the Ministerio de Educación of Spain for a supporting grant (reference AP2009-1739).

Received: 9 September 2014, **Revised:** 14 November 2014,

Accepted: 16 December 2014

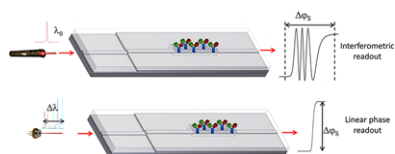
Published online:

Key words: Integrated optics, Biosensor, Interferometer, Phase modulation, Linear readout.

References

- [1] M. C. Estevez, M. Álvarez, and L. M. Lechuga, *Laser Photon. Rev.* **6**, 463–487 (2012).
- [2] P. Kozma, F. Kehl, E. Ehrentreich-Förster, C. Stamm, and F. F. Bier, *Biosens. Bioelectron.* **58**, 287–307 (2014).
- [3] R. G. Heideman, R. P. H. Kooyman, and J. Greve, *Sens. Actuators B* **10**, 209–217 (1993).
- [4] F. Prieto, B. Sepulveda, A. Calle, A. Llobera, C. Domínguez, A. Abad, A. Montoya, and L. M. Lechuga, *Nanotechnology* **14**, 907–912 (2003).
- [5] A. Brandenburg and R. Henninger, *Appl. Optics* **33**, 5941–5947 (1994).
- [6] A. Ymeti, J. S. Kanger, R. Wijn, P. V. Lambeck, and J. Greve, *Sens. Actuators B* **83**, 1–7 (2002).
- [7] K. Schmitt, B. Schirmer, C. Hoffmann, A. Brandenburg, and P. Meyrueis, *Biosens. Bioelectron.* **22**, 2591–2597 (2007).
- [8] B. H. Schneider, J. G. Edwards, and N. F. Hartman, *Clin. Chem.* **43**, 1757–1763 (1997).
- [9] B. H. Schneider, E. Dickinson, M. Vach, J. Hoijer, and L. Howard, *Biosens. Bioelectron.* **15**, 13–22 (2000).
- [10] K. A. Murphy, M. S. Miller, A. M. Vengsarkar, and R. O. Claus, *J. Lightwave Technol.* **8**, 1688–1696 (1990).
- [11] M. Spajer, *Opt. Lett.* **13**, 239–241 (1988).
- [12] A. M. Vengsarkar, W. C. Michie, L. Jankovic, B. Culshaw, and R. O. Claus, *J. Lightwave Technol.* **12**, 170–177 (1994).
- [13] J. Canning and A. Carter, *Opt. Lett.* **22**, 561–563 (1997).
- [14] R. X. Gao, Q. Wang, F. Zhao, B. Meng, and S. L. Qu, *Opt. Commun.* **283**, 3149–3152 (2010).
- [15] R. Poozesh, V. Vatani, M. Laffouti, K. Hejaz, R. Rezaei-Nasirabad, A. Babazadeh, S. H. Ghasemi, and J. Sabbaghzadeh, *Opt. Spectrosc.* **111**, 284–286 (2011).

- [16] R. Jha, J. Villatoro, G. Badenes, and V. Pruneri, *Opt. Lett.* **34**, 617–619 (2009).
- [17] T. Pinheiro-Ortega, E. Silvestre, P. Andres, B. Maes, and P. Bienstman, *IEEE Sens. J.* **10**, 1180–1184 (2010).
- [18] K. Zinoviev, A. B. González-Guerrero, C. Domínguez, and L. M. Lechuga, *J. Lightwave Technol.* **29**, 1926–1930 (2011).
- [19] U. Minoni, E. Sardini, E. Gelmini, F. Docchio, and D. Marioli, *Rev. Sci. Instrum.* **62**, 2579–2583 (1991).
- [20] B. Maisenhölder, H. P. Zappe, R. E. Kunz, P. Riel, M. Moser, and J. Edlinger, *Sens. Actuators B* **39**, 324–329 (1997).
- [21] R. Heideman and P. V. Lambeck, *Sens. Actuators B* **61**, 100–127 (1999).
- [22] V. Passaro, F. Magno, and A. Tsarev, *Opt. Express* **13**, 3429–3437 (2005).
- [23] B. Sepúlveda, G. Armelles, and L. M. Lechuga, *Sens. Actuators B* **134**, 339–347 (2007).
- [24] P. Kozma, A. Hamori, K. Cottier, S. Kurunczi, and R. Horvath, *Appl. Phys. B* **97**, 5–8 (2009).
- [25] A. Dér, S. Valkai, A. Mathesz, I. Andó, E. K. Wolff, and P. Ormos, *Sens. Actuators B* **151**, 26–29 (2010).
- [26] R. Halir, L. Vivien, X. Le Roux, D.-X. Xu, and P. Cheben, *IEEE Photon. J.* **5**, 6800906 (2013).
- [27] M. Kitsara, K. Misiakos, I. Raptis, and E. Makarona, *Opt. Express* **18**, 8193–8206 (2010).
- [28] M. La Notte and V. Passaro, *Sens. Actuators B* **176**, 994–1007 (2013).
- [29] T. Hutter, S. Elliott, and S. Ruschin, *Sens. Actuators B* **178**, 593–597 (2013).
- [30] K. Misiakos, I. Raptis, A. Salapatas, E. Makarona, A. Botzias, M. Hoekman, R. Stoffer, and G. Jobst, *Opt. Express* **22**, 8856–8870 (2014).
- [31] W. Bogaerts, P. De Heyn, T. Van Vaerenbergh, K. Le Vos, S. Kumar Selvaraja, T. Claes, P. Dumon, P. Bienstman, D. Van Thourhout, and R. Baets, *Laser Photon. Rev.* **6**, 47–73 (2012).
- [32] S. Dante, D. Duval, B. Sepúlveda, A. B. González-Guerrero, J. R. Sendra, and L. M. Lechuga, *Opt. Express* **20**, 7195–7205 (2012).
- [33] R. Levy and S. Ruschin, *Opt. Express* **25**, 20516–20521 (2008).
- [34] S. Tripathi, A. Kumar, E. Marin, and J.-P. Meunier, *IEEE Photon. Technol. Lett.* **22**, 799–801 (2010).
- [35] E. Salik, M. Medrano, G. Cohoon, J. Miller, C. Boyter, and J. Koh, *IEEE Photon. Technol. Lett.* **24**, 593–595 (2012).
- [36] P. Ridker, *Circulation* **107**, 363–369 (2003).
- [37] S. Mazer and L. Rabbani, *J. Thromb. Thrombolysis* **17**, 95–105 (2004).
- [38] A. B. González-Guerrero, M. Álvarez, A. García-Castaño, C. Domínguez, and L. M. Lechuga, *J. Colloid Interface Sci.* **393**, 402–410 (2013).
- [39] M. Bañuls, R. Puchades, and Á. Maquieira, *Anal. Chim. Acta* **777**, 1–16 (2013).
- [40] M. Soler, M. C. Estevez, M. Álvarez, M. Otte, B. Sepúlveda, and L. M. Lechuga, *Sensors* **14**, 2239–2258 (2014).
- [41] R. Gupta, A. Periyakaruppan, M. Meyyappan, and J. Koehne, *Biosens. Bioelectron.* **59**, 112–119 (2014).



To solve the ambiguities affecting interferometric biosensors, a phase modulation system based on variations of the incident wavelength and Fourier deconvolution is presented. The wavelength variation is introduced taking advantage of the power-wavelength dependence of commercial laser diodes, resulting in a cost-effective method, valid for all modal interferometers. Considering the modulation of a bimodal waveguide interferometric sensor, limits of detection of $4 \cdot 10^{-7}$ for bulk sensing and 7 ng/ml for the detection of C-Reactive protein were demonstrated.

Page 1–8

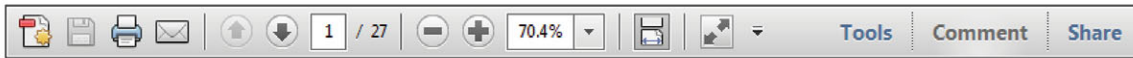
Stefania Dante, Daphné Duval, David Fariña, Ana Belén González-Guerrero, and Laura M. Lechuga
Linear readout of integrated interferometric biosensors using a periodic wavelength modulation

USING e-ANNOTATION TOOLS FOR ELECTRONIC PROOF CORRECTION

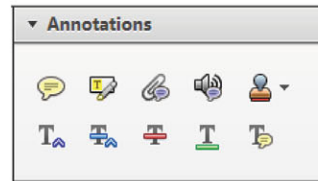
Required software to e-Annotate PDFs: **Adobe Acrobat Professional** or **Adobe Reader** (version 8.0 or above). (Note that this document uses screenshots from **Adobe Reader X**)

The latest version of Acrobat Reader can be downloaded for free at: <http://get.adobe.com/reader/>


Once you have Acrobat Reader open on your computer, click on the **Comment** tab at the right of the toolbar:



This will open up a panel down the right side of the document. The majority of tools you will use for annotating your proof will be in the **Annotations** section, pictured opposite. We've picked out some of these tools below:



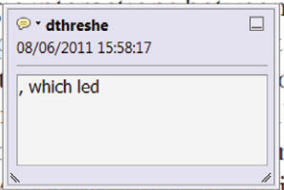
1. Replace (Ins) Tool – for replacing text.

 Strikes a line through text and opens up a text box where replacement text can be entered.


How to use it

- Highlight a word or sentence.
- Click on the **Replace (Ins)** icon in the Annotations section.
- Type the replacement text into the blue box that appears.

standard framework for the analysis of microeconomics. Nevertheless, it also led to the development of strategic form games. The number of competitors in a market is that the structure of the game is a main component. In a Cournot duopoly, the main components are the number of firms, the important works on entry by Cournot (1838) henceforth) we open the 'black b



2. Strikethrough (Del) Tool – for deleting text.

 Strikes a red line through text that is to be deleted.

How to use it

- Highlight a word or sentence.
- Click on the **Strikethrough (Del)** icon in the Annotations section.

there is no room for extra profits as mark-ups are zero and the number of firms (n) values are not determined by the market. Blanchard and Kiyotaki (1987), perfect competition in general equilibrium. The effects of aggregate demand and supply shocks in a classical framework assuming monopolistic competition and an exogenous number of firms

3. Add note to text Tool – for highlighting a section to be changed to bold or italic.

 Highlights text in yellow and opens up a text box where comments can be entered.

How to use it

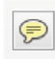
- Highlight the relevant section of text.
- Click on the **Add note to text** icon in the Annotations section.
- Type instruction on what should be changed regarding the text into the yellow box that appears.

dynamic responses of mark-ups are consistent with the VAR evidence

sation of the VAR with the VAR evidence. The VAR model is well suited to the analysis of the dynamic responses of mark-ups to a shock in the demand.



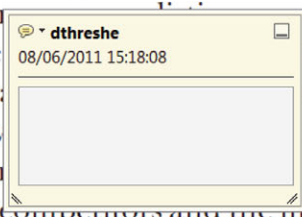
4. Add sticky note Tool – for making notes at specific points in the text.

 Marks a point in the proof where a comment needs to be highlighted.

How to use it

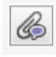
- Click on the **Add sticky note** icon in the Annotations section.
- Click at the point in the proof where the comment should be inserted.
- Type the comment into the yellow box that appears.

and supply shocks. Most of the literature on the dynamic responses of mark-ups to a shock in the demand is based on the standard framework. The VAR model is well suited to the analysis of the dynamic responses of mark-ups to a shock in the demand. The VAR model is well suited to the analysis of the dynamic responses of mark-ups to a shock in the demand.



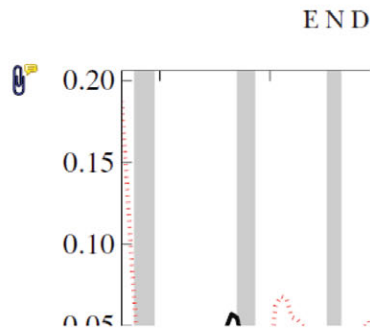
USING e-ANNOTATION TOOLS FOR ELECTRONIC PROOF CORRECTION

5. Attach File Tool – for inserting large amounts of text or replacement figures.


 Inserts an icon linking to the attached file in the appropriate place in the text.

How to use it

- Click on the **Attach File** icon in the Annotations section.
- Click on the proof to where you'd like the attached file to be linked.
- Select the file to be attached from your computer or network.
- Select the colour and type of icon that will appear in the proof. Click OK.



6. Add stamp Tool – for approving a proof if no corrections are required.

 Inserts a selected stamp onto an appropriate place in the proof.

How to use it

- Click on the **Add stamp** icon in the Annotations section.
- Select the stamp you want to use. (The **Approved** stamp is usually available directly in the menu that appears).
- Click on the proof where you'd like the stamp to appear. (Where a proof is to be approved as it is, this would normally be on the first page).

of the business cycle, starting with the
 on perfect competition, constant ret
 production. In this environment goods
 extra profit is due to the fact that the
 he profit is determined by the model. The New-Key
 otaki (1987), has introduced produc
 general equilibrium models with nomin
 and real variables. Most of his work

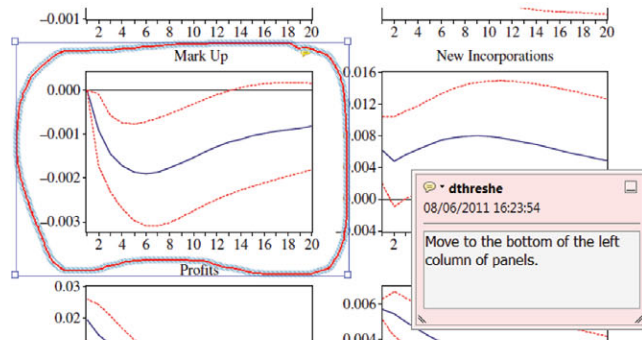


7. Drawing Markups Tools – for drawing shapes, lines and freeform annotations on proofs and commenting on these marks.

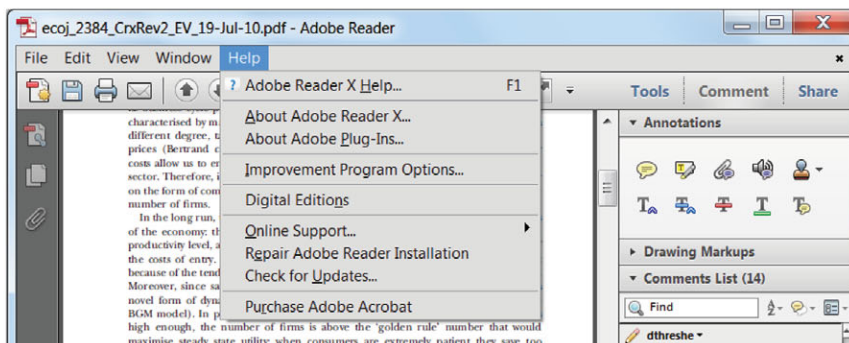
Allows shapes, lines and freeform annotations to be drawn on proofs and for comment to be made on these marks..

How to use it

- Click on one of the shapes in the **Drawing Markups** section.
- Click on the proof at the relevant point and draw the selected shape with the cursor.
- To add a comment to the drawn shape, move the cursor over the shape until an arrowhead appears.
- Double click on the shape and type any text in the red box that appears.



For further information on how to annotate proofs, click on the **Help** menu to reveal a list of further options:



Instructions for Proof Corrections and Orders



2014 WILEY-VCH GmbH & Co. KGaA
Laser & Photonics Reviews
Rotherstrasse 21
10245 Berlin
Germany

WILEY-VCH

TEL +49 (0) 30-47 03 13 21
FAX +49 (0) 30-47 03 13 99
E-MAIL laser@wiley-vch.de

Please correct your proofs and return them within 5 days together with the completed reprint order form. The editors reserve the right to publish your article with editors' corrections if your proofs do not arrive in time.

After having received your corrections, your paper will be published online soon in the Wiley Online Library (wileyonlinelibrary.com).

Please keep in mind that reading proofs is your responsibility. Corrections should therefore be clear. We prefer the corrections be made directly within the PDF file (see E-annotations instructions). Alternatively, you may provide us with a list of corrections by e-mail, with the corrections referring to their line number.

Manuscript files are sometimes slightly modified by the production department to follow general presentation rules of the journal.

Note that the quality of the halftone figures is not as high as the final version that will appear in the issue.

Check the enclosed proofs very carefully, paying particular attention to the formulas (including line breakings introduced in production), figures, numerical values, tabulated data and layout of the pages.

A black box (■) or a question at the end of the paper (after the references) signals unclear or missing information that specifically requires **your attention**. Note that the author is liable for damages arising from incorrect statements, including misprints.

The main aim of proofreading is to correct errors that may have occurred during the production process, **and not to modify the content of the paper**. Corrections that may lead to a change in the page layout should be avoided.

Note that sending back a corrected **manuscript file is of no use**.

Return the corrected proofs within 5 days by e-mail.

Please do not send your corrections to the typesetter but to the Editorial Office:

E-MAIL laser@wiley-vch.de

Please limit corrections to errors in the text; cost incurred for any further changes or additions will be charged to the author, unless such changes have been agreed upon by the editor.

If your paper contains **color figures**, please fill in the Color Print Authorization and note the further information given on the following pages.

Full color reprints, Customized PDF files, Printed Issues, Color Print, and Cover Posters may be ordered by filling in the accompanying form.

Contact the Editorial Office for **special offers** such as

- Personalized and customized reprints (e.g. with special cover, selected or all your articles published in Wiley-VCH journals)
- Cover/frontispiece publications and posters (standard or customized)
- Promotional packages accompanying your publication

Visit the **MaterialsViews.com Online Store** for a wide selection of posters, logos, prints and souvenirs from our top physics and materials science journals at www.cafepress.com/materialsviews

Order Form

2014 WILEY-VCH GmbH & Co. KGaA
Laser & Photonics Reviews
Rotherstrasse 21
10245 Berlin
Germany

WILEY-VCH

Article No.

Author/Title

e-mail address

TEL +49 (0) 30-47 03 13 21
FAX +49 (0) 30-47 03 13 99
E-MAIL laser@wiley-vch.de

**Please complete
this form and return
it by e-mail or FAX.**

Required Fields may be filled in using Adobe Reader

Color Print Authorization

Please bill me for

color print figures (total number of color figures)

YES, please print Figs. No. in color.

NO, please print all color figures in black/white.

Reprints/Issues/PDF Files/Posters

Whole issues, reprints and PDF files (300 dpi) for an unlimited number of printouts are available at the rates given on the next page. Reprints and PDF files can be ordered before and after publication of an article. All reprints will be delivered in full color, regardless of black/white printing in the journal.

Reprints

Please send me and bill me for

full color reprints with color cover

full color reprints with personalized color cover

Issues

Please send me and bill me for

entire issues

Customized PDF-Reprint

Please send me and bill me for

a PDF file (300 dpi) for an unlimited number of printouts with customized color cover sheet.

The PDF file will be sent to your e-mail address.

Send PDF file to:

Please note that posting of the final published version on the open internet is not permitted. For author rights and re-use options, see the Copyright Transfer Agreement at <http://www.wiley.com/go/ctavchglobal>.

Cover Posters

Posters are available of all the published covers in two sizes (see attached price list). Please send me and bill me for

A2 (42 × 60 cm/17 × 24in) posters

A1 (60 × 84 cm/24 × 33in) posters

Mail reprints and/or issues and/or posters to (no P.O. Boxes):

VAT number:

Information regarding VAT

Please note that from German sales tax point of view, the charge for **Reprints, Issues or Posters** is considered as "supply of goods" and therefore, in general, such delivery is subject to German VAT. However, this regulation has no impact on customers located outside of the European Union. Deliveries to customers outside the Community are automatically tax-exempt. Deliveries within the Community to institutional customers outside of Germany are exempted from German tax (VAT) only if the customer provides the supplier with his/her VAT number.

The VAT number (value added tax identification number) is a tax registration number used in the countries of the European Union to identify corporate entities doing business there. It starts with a country code (e.g. FR for France, GB for Great Britain) and follows by numbers.

The charges for publication of **front/back/inside cover pictures, color figures or frontispieces** are considered to be "supply of services" and therefore subject to German VAT. However, if you are an institutional customer outside Germany, the tax can be waived if you provide us with the VAT number of your company. Non-EU customers may have a VAT number starting with "EU" instead of their country code if they are registered with the EU tax authorities. If you do not have an EU VAT number and you are a taxable person doing business in a non-EU country, please provide certification from your local tax authorities confirming that you are a taxable person under local tax law. Please note that the certification must confirm that you are a taxable person and are conducting an economic activity in your country. **Note:** Certifications confirming that you are a tax-exempt legal body (non-profit organization, public body, school, political party, etc.) in your country do not exempt you from paying German VAT.

Purchase Order No.:

Terms of payment:

Please send an invoice Cheque is enclosed

VISA, MasterCard and AMERICAN EXPRESS.

Please use this link (Credit Card Token Generator) to create a secure Credit Card Token and include this number in the form instead of the credit card data.

https://www.wiley-vch.de/editorial_production/index.php

CREDIT CARD TOKEN NUMBER:

<input type="text"/>	<input type="text"/>	<input type="text"/>	<input type="text"/>	<input type="text"/>	<input type="text"/>	<input type="text"/>	<input type="text"/>	<input type="text"/>	<input type="text"/>	<input type="text"/>	<input type="text"/>	<input type="text"/>	<input type="text"/>	<input type="text"/>	<input type="text"/>	<input type="text"/>	<input type="text"/>	<input type="text"/>	<input type="text"/>
----------------------	----------------------	----------------------	----------------------	----------------------	----------------------	----------------------	----------------------	----------------------	----------------------	----------------------	----------------------	----------------------	----------------------	----------------------	----------------------	----------------------	----------------------	----------------------	----------------------

Send invoice to:

Signature _____

Date _____

Please use this form to confirm that you are prepared to pay your contribution.

Please sign and return this page.

You will receive an invoice following the publication of your article in the journal issue.

Price List – Laser & Photonics Reviews 2014

WILEY-VCH

Reprints/Issues/PDF-Files/Posters

The prices listed below are valid only for orders received in the course of 2014. Minimum order for reprints is 50 copies. **Reprints can be ordered before *and after* publication of an article. All reprints are delivered with color cover and color figures.** If more than 500 copies are ordered, special prices are available upon request.

Single issues are available to authors at a reduced price.

The prices include mailing and handling charges. All prices are subject to local VAT/sales tax.

Reprints with color cover Size (pages)	Price for orders of (in Euro)					
	50 copies	100 copies	150 copies	200 copies	300 copies	500 copies*
1–4	345	395	425	445	548	752
5–8	490	573	608	636	784	1077
9–12	640	739	786	824	1016	1396
13–16	780	900	958	1004	1237	1701
17–20	930	1070	1138	1196	1489	2022
for every additional 4 pages	147	169	175	188	231	315
for personalized color cover	190	340	440	650	840	990
PDF file (300 dpi, unlimited number of printouts, customized cover sheet) € 330						
Issues	€ 36 per copy for up to 10 copies.*					
Cover Posters	• A2 (42 × 60 cm/17 × 24in)	€ 49				
	• A1 (60 × 84 cm/24 × 33in)	€ 69				

*Prices for more copies available on request.

Special offer: If you order 100 or more reprints you will receive a pdf file (300 dpi, unlimited number of printouts, color figures) and an issue for free.

Color figures

If your paper contains **color figures**, please notice that, generally, these figures will appear in color in the online PDF version and all reprints of your article at no cost. The print version of the figures in the journal hardcopy will be black/white unless the author explicitly requests a color print publication and contributes to the additional printing costs.

Approximate color print figure charges	
First figure	€ 495
Each additional figure	€ 395 Special prices for more color print figures on request

If you wish color figures in print, please answer the **color print authorization** questions on the order form.